ORIGINAL ARTICLE

Preparation, Characterization, and Application of Electrospun BAG/CMC/β-CD Nanofibers for Flutamide Drug Delivery

Masoumeh Tajik[1] · Mirabdullah Seyed-Sadjadi[1] ⬤ · Karim Zare[1] · Nazanin Farhadyar[2]

Abstract

In this study, using a combination of bioactive glass (BAG), carboxymethyl cellulose (CMC), and β-cyclodextrin (β-CD), a novel nanofiber network was fabricated through the electrospinning method. The biocompatible BAG/CMC/β-CD nanofibers (NF) were optimized for the controlled release of flutamide, a hydrophobic anticancer drug, which was immobilized on the surface of nanofibers through chemical conjugation. The synthesized nanofibers were characterized by various analytical techniques, including X-ray diffraction analysis, Fourier-transform infrared spectroscopy, X-ray photoelectron spectroscopy, the Brunauer–Emmett–Teller specific surface area, field emission scanning electron microscopy, energy dispersive X-ray spectroscopy, transmission electron microscopy, and UV–Vis Spectroscopy. The drug loading and in vitro drug release studies at a pH of 7.4 investigated the high loading efficiency at 99.65% and the release without an initial burst of a high dosage of the drug in a few hours. The drug release achieved 100% within 12 h, following a sustained release pattern due to the slow degradation of the matrix. The findings suggest that BAG/CMC/β-CD NF could be a promising candidate for the flutamide drug delivery system due to overcoming the challenges of its poor bioavailability and low aqueous solubility.

Keywords Bioactive glass · CMC · β-cyclodextrin · Electrospinning · Nanofibers

Introduction

In recent years, bioactive glasses (BAGs) have gained much attention for delivering pharmaceutical compounds in the human body due to their unique properties, such as a strong bonding with the biological systems, nanoporous, semiconducting, adhesive, and antibacterial effects [1]. While many investigations have been conducted on bioactive glasses, previous studies have identified several constraints, such as slow drug loading and fast drug release [2]. Researchers have suggested that these limitations can be resolved by improving the fabrication methods. BAGs, which are composed of the elements commonly found in the body like silicon, calcium, phosphorus, sodium, potassium, magnesium, and oxygen, form a mechanically strong bone and soft tissue bonding while implanted or in contact

with the biological fluids [3–6]. As a result, BAGs are easily absorbed, degraded, and degenerated through hydrogen exchange in the biological fluids, which leads to the alkalinity of the environment [7–9]. The shift to a more alkaline environment can be stressful for bacteria. Zhang et al. attributed the antibacterial activity of BAGs to the increase in pH level. The exchange of sodium ions with protons in the body fluids increases the local pH to 11 within 8 h, remaining for more than 48 h [10]. Furthermore, the silica, calcium, and phosphate ions in BAGs can disrupt the membrane potential of bacteria and create a higher osmotic pressure, inducing morphological changes such as cell shrinkage, reduction of cell dimensions, and damage to bacterial membranes, as emphasized by Drago et al. [11]. It is interesting to note that incorporating therapeutic ions such as copper and zinc into the structure of BAGs enhances their antibacterial properties [12]. Therefore, different types of antibacterial ion-doped and drug-loaded BAGs have been globally introduced and discussed as drug delivery systems, along with the significant challenges ahead.

Various methods, such as the flame method, microwave irradiation, microemulsion, and melt-quenching process, synthesize BAGs in a short time, about several hours, by

✉ Mirabdullah Seyed-Sadjadi
  mirabdullahseyedsadjadi@gmail.com

1 Department of Chemistry, Science and Research Branch, Islamic Azad University, Tehran, Iran

2 Department of Chemistry, Varamin Pishva Branch, Islamic Azad University, Tehran, Iran

heating the initial precursors. However, the outcome is a product with a low specific surface area [13–18]. According to the previous investigations, the specific surface area value significantly affects the bioactive glasses function. The main procedure to synthesize highly bioactive glasses is the sol–gel method. It improves the crystal growth of the product, modifies the specific surface area, and increases porosity and apatite-forming ability compared to the other fabrication methods, which have the advantage of higher mechanical properties [19–21]. Nanofibers, with numerous potentials in biomedical applications such as tissue engineering, drug delivery, and cancer diagnosis, can be generated from BAGs through electrospinning, which makes them versatile [22]. Electrospinning is a simple, inexpensive, and user-friendly method to fabricate ultrathin fibers with controllable diameters, compositions, orientations, and high surface-to-volume ratios. It uses an electrical charge to draw very fine and continuous nanofibers from a liquid solution. With the development of electrospinning techniques, a diverse range of materials, including natural polymers, synthetic polymers, and their composites, have been transformed into ultrathin fibers [23]. Due to their superior adhesiveness to biological surfaces, nanofibers are ideal candidates for drug delivery systems. To develop nanofibers with the desired drug release kinetics, it is crucial to carefully select the appropriate polymer, the solvent, and the electrospinning setup. A study by Mostafa et al. involved the combination of an organic, water-soluble polymer blend, chitosan/polyvinyl alcohol, and an inorganic BAG as a drug delivery system for a model osteoporotic drug [24]. Water-soluble polymers are suitable for immediate drug release due to their rapid dissolution, while biodegradable polymers are better suited for prolonged or sustained drug release. Biodegradable polymers are designed to break down through natural metabolic mechanisms in the body, which makes them much less toxic compared to synthetic polymers [25].

Carboxymethyl cellulose (CMC), a derivative of cellulose, is a type of water-soluble biodegradable polymer, widely utilized in the food, pharmaceutical, and biomedical industries. It has a great tendency to form covalent bonds with the amine groups of drugs owing to carboxymethyl groups. Due to its polymeric structure and the ability of the carboxyl group, CMC has found its way into pharmaceutical formulations and drug delivery systems. The biological half-life of drugs attached to CMC extends, leading to less frequent drug taking [26].

β-cyclodextrin (β-CD) is another type of water-soluble biodegradable polymer which is derived from starch. It is of great interest in the biomedical, food and agricultural industries because of its ability to interact with surfactants and form complexes with different types of molecules. β-CD has a unique structure for solubilizing, stabilizing, and delivering hydrophobic drugs. It consists of four macrocyclic rings that form a sort of tour-like shape. The hydroxyl groups are located at the top and bottom of the tours, while CH_2 groups fill the center of the tour to create a hydrophobic cavity. The free carboxylic acid groups around the β-CD hydrophobic cavity allow it to encapsulate anticancer agents and poorly water-soluble drugs like flutamide, protect them from physicochemical degradation, deliver them by controlling pH within the physiological range, and extend their release [27].

Flutamide is a hydrophobic prostate anticancer drug. Its mechanism of action involves competing with testosterone and dihydrotestosterone for binding to androgen receptors in tissues. Flutamide is available as oral tablets with poor bioavailability due to its low aqueous solubility and rapid first-pass hepatic extraction with a short half-life of 5–6 h. So, a wetting agent like sodium lauryl sulfate is added to flutamide tablets to improve its dissolution rate. However, due to the limitations of its current formulation, there is a growing interest in finding a novel delivery system to overcome these challenges [28].

This work presents the synthesis of novel electrospun nanofibers through the sol–gel method based on a blend of BAG, CMC, and β-CD for a favorable flutamide drug delivery system. The control of pH, temperature, stirring rate, and exiting speed of the reaction solution in the electrospinning process led to the fabrication of the biocompatible and biodegradable BAG/CMC/β-CD nanofibers. Then, the flutamide drug was loaded and chemically bound to the electrospun BAG/CMC/β-CD NF, and the in vitro drug release was further studied. The crystalline and chemical structures, morphologies, and characteristics of the synthesized samples in drug loading and release were characterized by various analytical techniques. Due to the aggregate properties of components, the BAG/CMC/β-CD nanofibers resulted in a high loading capacity and slow-release ability, ideal for long-term and lower-dose flutamide administration.

Experimental

Materials

All the chemical reagents, including carboxymethyl cellulose ($C_8H_{16}O_8$, 240.21 g/mol), beta-cyclodextrin (β-CD) ($C_{42}H_{70}O_{35}$, 1320 g/mol), tetraethyl orthosilicate (TEOS) ($SiC_8H_{20}O_4$, 208.33 g/mol), calcium nitrate (CaN_2O_6, 164.09 g/mol), sodium nitrate ($NaNO_3$, 84.99 g/mol), ammonium dihydrogen phosphate (ADP) ($NH_4H_2PO_4$, 115.03 g/mol), polyvinyl alcohol (PVA) ($C_{2n}H_{4n}O_n$, 44.05 g/mol), and hydrochloric acid (HCl, 36.46 g/mol) were purchased from Merck Co. (Germany), while analytical grade and chemically purified. The flutamide anti-cancer drug ($C_{11}H_{11}F_3N_2O_3$, 276.21 g/mol) was prepared from Sobhan

Pharmaceutical Chemistry Co. (Iran). The deionized water was produced in the lab.

Synthesis

Synthesis of Bioactive Glass/Carboxymethyl Cellulose/β-Cyclodextrin (BAG/CMC/β-CD NC)

The BAG/CMC/β-CD nanobioceramics were synthesized using the sol–gel method. To begin with, a mixture of 2 g carboxymethyl cellulose and 2 g β-cyclodextrin was dispersed in DI water using ultrasonication. The mixture was then heated at 80 °C with magnetic stirring for 60 min while adjusting pH to 2 using hydrochloric acid. Next, 20 mL tetraethyl orthosilicate was added to the solution and mixed with stirring for 60 min at room temperature. This was followed by adding 8.75 g calcium nitrate, 6.75 g sodium nitrate, and 1.2 g ammonium dihydrogen phosphate to the above suspension and stirring it for 60 min. The mixture was then ultrasonically stirred for another 60 min. Finally, the jelly-like product of BAG/CMC/β-CD was dried in an oven at 100 °C for 3 h, well-ground, and kept for further use. The BAG/CMC and BAG/β-CD nanobioceramics were fabricated with 2 g carboxymethyl cellulose and 2 g β-cyclodextrin, respectively, following the above synthesis route.

Synthesis of BAG/CMC/β-CD NF

The synthesized BAG/CMC/β-CD powder was dissolved in PVA solution and placed in 5 ml syringes with a metal capillary (2 mm diameter). The syringes were then applied to the electrospinning machine ES 1000 for 3–4 h to spin nanofibers on the aluminum foil collector. Several tests were conducted to determine the optimal parameters for producing the desired nanofibers with the least amount of knots.

The distance between the tip of the syringe capillary and the counter electrode was set to 11–12 cm, and the exit speed of the solution was 0.4 mL/h. The applied voltages varied from 15 to 20 kV, with an average of 17 kV. After electrospinning, the nanofibers were exposed to steam for 24 h and then kept in an incubator. The process is schematically illustrated in Fig. 1.

Electrospun BAG/CMC/β-CD NF as Drug Delivery System

Due to high surface area-to-volume ratios, efficient delivery of hydrophilic and hydrophobic drugs, ease of operation, and cost-effectiveness, electrospun nanofibers are an excellent choice for wound dressing and local cancer treatments. By modifying specific parameters such as the diameter, morphology, and porosity of nanofibers, the drug release profile can be altered to meet specific medical requirements. To achieve the desired drug release kinetics, a suitable method of drug loading should be designed. Previous studies mainly focused on the encapsulation of drugs within the nanofiber networks. However, by introducing surface-modified designs for drug loading, it is now possible to construct more advanced drug delivery platforms [29, 30]. In this study, the flutamide drug was loaded and chemically bound to the electrospun BAG/CMC/β-CD NF, as shown in Fig. 2. The scanning electron micrograph of flutamide-loaded BAG/CMC/β-CD NF attests to the perfect inclusion of the flutamide drug on the surface of the electrospun nanoporous fibers.

Drug Loading Studies

According to the procedure, 1 mg flutamide was dissolved in 2.5 mL methanol and added to 150 mL phosphate buffer
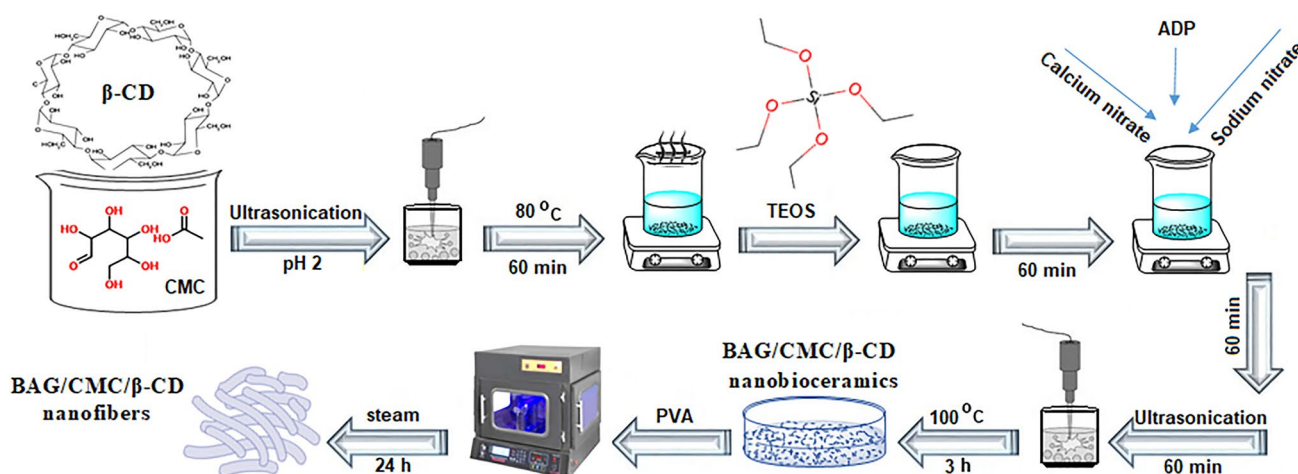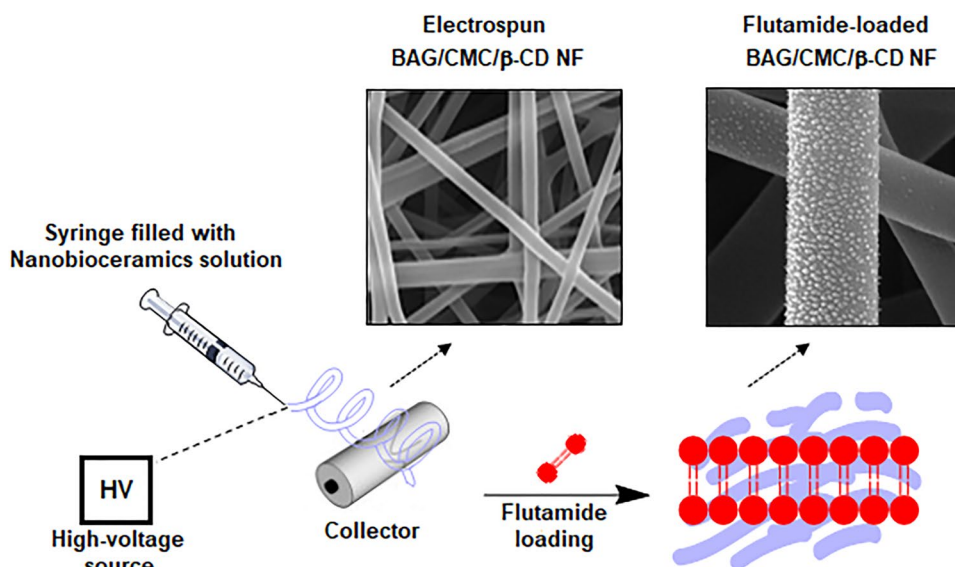

Fig. 1 Schematic illustration for the preparation of BAG/CMC/β-CD NF

Fig. 2 Electrospun BAG/CMC/β-CD NF as drug delivery system

with a pH of 7.4. Then, 3 mg BAG/CMC/β-CD NF was mixed with the solution and stirred for 24 h at 5000 rpm using a magnetic stirrer. After centrifugation, the absorbance of the supernatant was measured at $\lambda_{max} = 282$ nm using a UV–Vis spectrophotometer. By subtracting this value from the initial concentration of flutamide, the drug loading capacity in BAG/CMC/β-CD NF was determined.

Drug Release Studies

An in vitro flutamide release study was performed by adding 6 mg of the freeze-dried flutamide-loaded BAG/CMC/β-CD NF to 10 mL phosphate buffer with a pH of 7.4, mixed for 45 min under gentle shaking. The drug release studies continued for 8 h, and at certain time intervals (every 1 h), 0.5 ml samples of the dissolution medium were withdrawn, centrifuged, and assayed at 282 nm. Then, drug release studies were repeated every 4 h until 40 h following the same protocol. The ratio of released flutamide at a particular time point to the maximum released amount determined the release efficiency.

Characterization

XRD Analysis

X-ray diffraction (XRD) analysis was carried out on the PANALYTICAL X'PERT PRO X-ray diffractometer (United Kingdom) using Cu-Kα radiation ($\lambda = 1.54$ Å) with a scanning angle (2θ) from 10° to 80°. Since the instrument was a powder X-ray diffractometer, samples were prepared in powder form using a rotary motion with a mortar and pestle. The finer the powder, the better the data. The XRD patterns

were compared with the analysis data in the Joint Committee on Powder Diffraction Standards (JCPDS).

FT-IR Analysis

Fourier-transform infrared (FT-IR) spectra were recorded on a PerkinElmer FT-IR spectrophotometer (USA) within the 4000–500 cm^{-1} range. Samples were prepared through the KBr method. About 1 mg sample was uniformly blended with 300 mg potassium bromide (KBr) and pressed into a pellet.

XPS Analysis

X-ray photoelectron spectroscopy (XPS) spectra were taken from a BESTEC EA 10 spectrometer (Germany) using an Al-Kα source. Just before XPS analysis, the finely powdered sample was pressed onto the surface of the sample stage by using a freshly cleaned spatula.

BET Analysis

The Brunauer–Emmett–Teller (BET) specific surface area and pore-size distribution data were collected on the BEL-SORP MINI II, manufactured by the BEL Co., Japan. Before BET analysis, the sample was degassed at 120 °C for 2 h to lose water vapor, carbon dioxide, or other molecules that might occupy the volume of the material's cavities. Then, the BET surface area measurement was obtained by the adsorption and desorption isotherms of nitrogen at − 196 °C (the liquid nitrogen temperature), using a single-point method.

FESEM and EDX Analyses

Field emission scanning electron microscopy (FESEM) and Energy dispersive X-ray spectroscopy (EDX) were checked by a TESCAN VEGA3 XMU instrument (Czech Republic) at the acceleration voltage of 20 kV. Samples were prepared by coating with a thin layer of gold (Au).

TEM Analysis

Transmission electron microscopy (TEM) images were obtained using the Zeiss-EM10C-100 kV apparatus (Germany). The sample was cut into ultra-thin and semi-transparent sections using a diamond knife.

UV–Vis Analysis

UV–Vis absorption spectra were obtained by the GBC CINTRA 20 double-beam spectrophotometer (Australia) to investigate flutamide loading and in vitro release efficiencies. The absorbance of the solutions was measured at 282 nm.

Results and Discussion

Structural Analysis

The crystallographic structures of BAG/CMC, BAG/β-CD, BAG/CMC/β-CD NCs, and BAG/CMC/β-CD NF, using XRD diffraction patterns, are shown in Fig. 3. The chemical structure and crystal form of samples are verified by the peak position and peak width of XRD signals. The XRD pattern of BAG/CMC NC shows a strong peak, centered at 29.51°, corresponding to the (121) reflection. The other five peaks found at 26.03°, 32.01°, 35.49°, 39.08°, and 48.04° are well indexed to the (002), (211), (200), (221), and (231) crystal planes of BAG/CMC NC, respectively, according to the standard JCPDS cards (09-0432), (34-0189), and (11-0273) [31, 32]. Furthermore, some small peaks that may be related to the formation of the bioactive glass-ceramic samples can be detected according to the standard JCPDS cards (09-0169) and (19-0248) [33]. This diffraction pattern is observed at BAG/β-CD NC as well, but it is slightly stronger compared to that of the BAG/CMC NC sample. In the case of BAG/CMC/β-CD NC, the crystal planes with less intensity are present. The XRD spectrum of BAG/CMC/β-CD NF displays a distinct broad peak centered at 19.56°, which arises from the (102) monophasic diffraction plane of amorphous bioactive glass
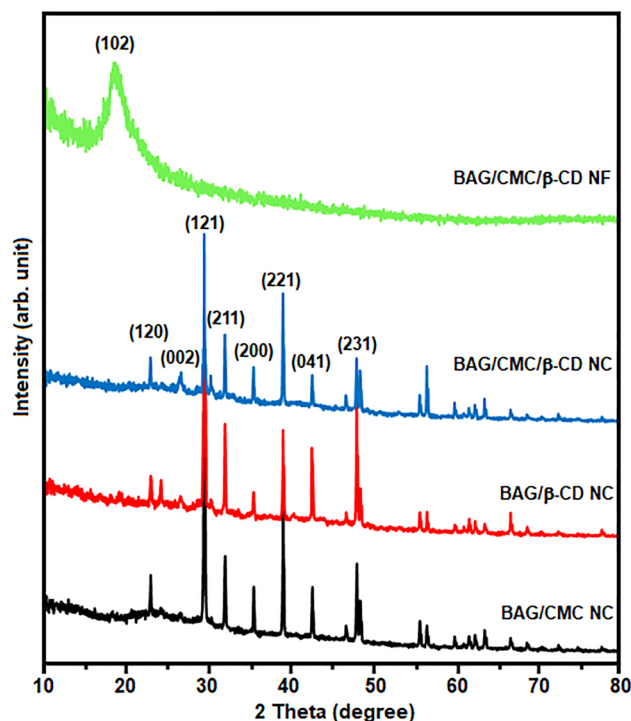
Fig. 3 XRD patterns of BAG/CMC NC, BAG/β-CD NC, BAG/CMC/β-CD NC, and BAG/CMC/β-CD NF

Table 1 Average crystallite size of samples using XRD diffraction peaks

| Sample	Crystallite size (nm)
BAG/CMC NC	61
BAG/β-CD NC	69
BAG/CMC/β-CD NC	66
BAG/CMC/β-CD NF	4

nanofibers due to the existence of PVA (JCPDS file No. 41-1049) [34, 35]. The following Debye–Scherrer equation is used to estimate the average crystallite size of the samples:

$$D = k \lambda / \beta \cos \theta \qquad (1)$$

where D is the crystallite size (nm), k is a constant of 0.94, λ is the X-ray radiation wavelength (0.15418 nm), β is the full width at half maximum (FWHM) of the peaks (radians), and θ is their diffraction angle (radians). The average crystallite sizes of BAG/CMC, BAG/β-CD, BAG/CMC/β-CD NCs, and BAG/CMC/β-CD NF, roughly calculated, are presented in Table 1. It can be seen that the crystal size of the BAG/CMC/β-CD NF decreased compared to that of BAG/CMC/β-CD NC. The reason is attributed to the cross-linking

Fig. 4 FT-IR spectra of BAG/CMC NC, BAG/β-CD NC, BAG/CMC/β-CD NC, and BAG/CMC/β-CD NF
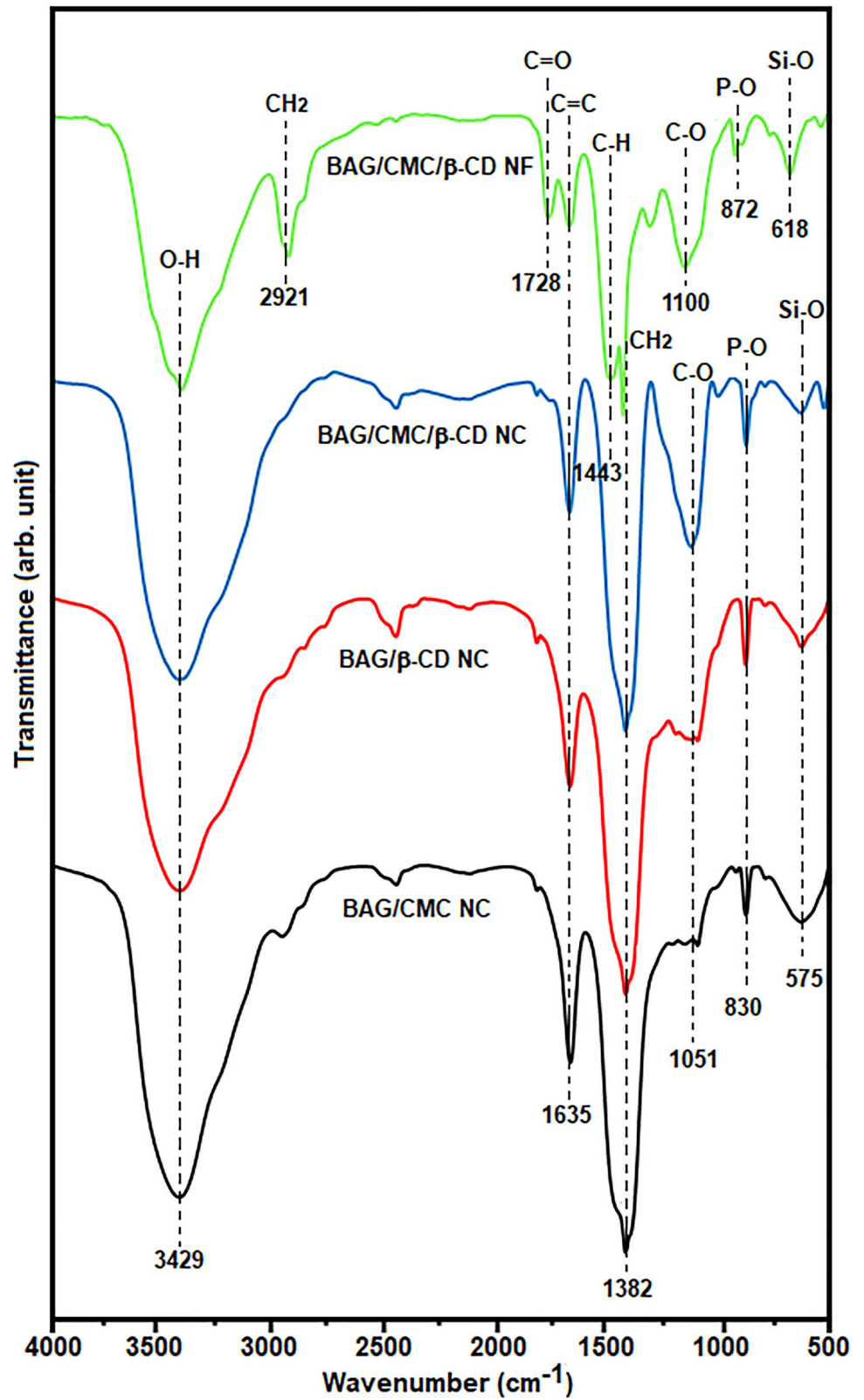
of PVA, which destroyed the regularity of bioactive glass nanofibers, resulting in smaller crystals [36].

Chemical Analyses

The chemical structures and functional groups of BAG/CMC, BAG/β-CD, BAG/CMC/β-CD NCs, and BAG/CMC/β-CD NF, using FT-IR spectroscopy, are presented in Fig. 4. The bonds between elements, characterized by infrared transmittance intensity at certain wavenumbers, prove the formation of nanostructures. As shown, the absorption bands at 575 and 618 cm^{-1} are assigned to the stretching vibrations of the Si–O bands and bending vibration of SiO$_4$ groups in silicate chains [37], while the stretching vibration of Si–O–Si band is found at 791 cm^{-1} [38]. The peaks at 830 and 872 cm^{-1} are associated with the stretching vibration bands of PO$_4$ [39]. The peaks at 1051 and 1100 cm^{-1} are associated with the C–O stretching motion. The peaks at 1382 cm^{-1} and 1443 cm^{-1} arise from the CH$_2$ out-of-plane bending vibration and C–H bending vibration, respectively. The peak at 1635

is ascribed to the presence of C=C stretching mode. In the FT-IR spectrum of BAG/CMC/β-CD nanofibers, two peaks are observed at 1728 and 2921 cm^{-1} due to the C=O and C–O from the acetate group remaining from PVA and the asymmetric stretching of CH$_2$, respectively. Moreover, four synthesized samples have the distinctive O–H vibration from the adsorbed water at 3429 cm^{-1} [34, 40].

The chemical compositions of BAG/CMC, BAG/β-CD, BAG/CMC/β-CD NCs, and BAG/CMC/β-CD NF, evaluated through the EDX spectra, are shown in Fig. 5a–d. The elemental analyses confirm the presence of the expected elements of N, O, Na, Si, P, S, and Ca with the proper energy level. The basic composition and weight percentage of the elements are listed in Table 2. The insets of Fig. 5a–c exhibit the shape of nanobioceramic during synthesis, while the inset of Fig. 5d displays the electrospun nanofibers collected on a foil. Figure 5e shows the elemental graphs of BAG/CMC/β-CD NF.

The elemental compositions and surface chemical states of BAG/CMC/β-CD NF, examined by X-ray photoelectron spectroscopy (XPS) within a range of binding energies of
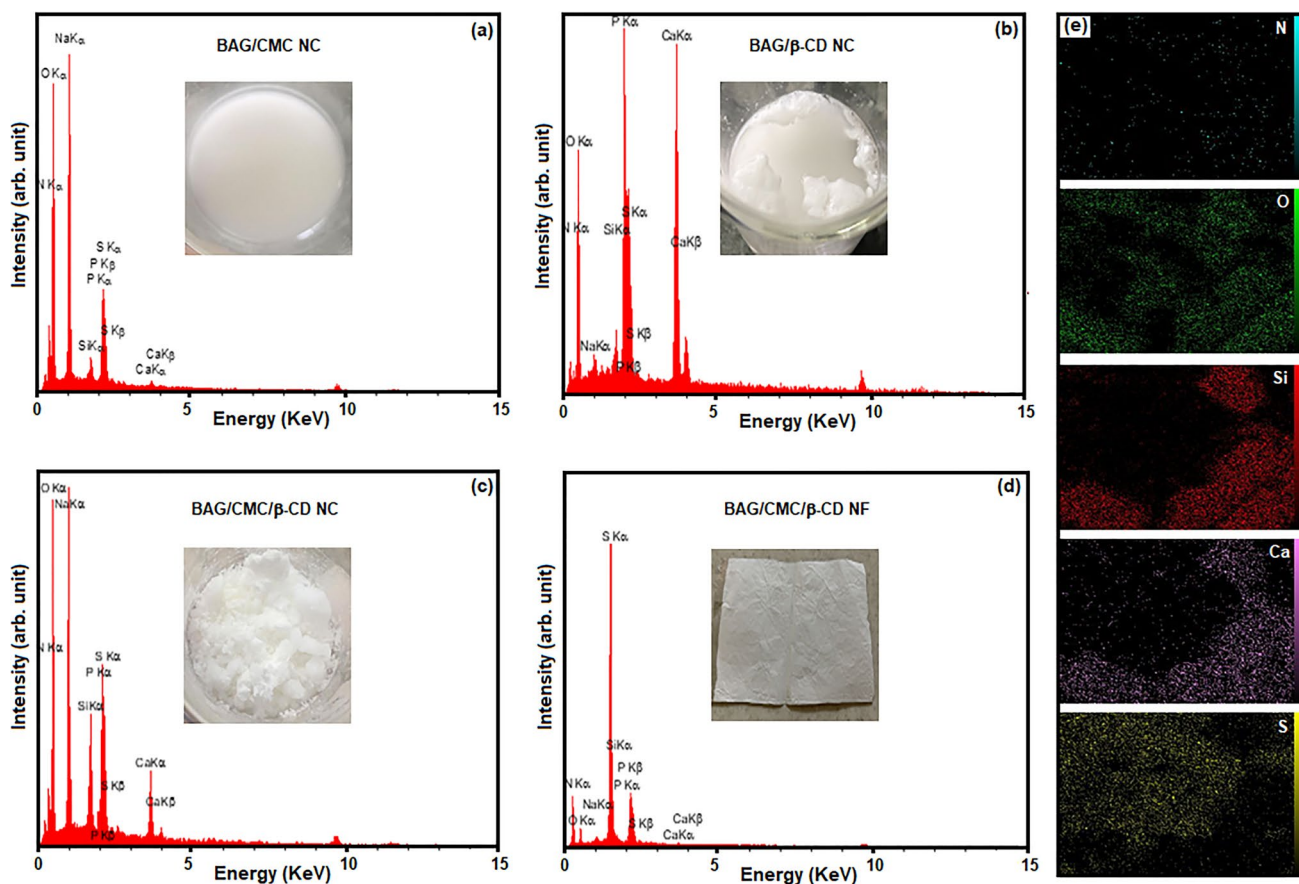
Fig. 5 EDX spectra of **a** BAG/CMC NC, **b** BAG/β-CD NC, **c** BAG/CMC/β-CD NC, and **d** BAG/CMC/β-CD NF. **e** Elemental graphs of BAG/CMC/β-CD NF. The insets of figures (**a**–**c**) exhibit the shape of nanobioceramics during synthesis, while the inset of figure (**d**) displays the electrospun nanofibers collected on a foil

Table 2 The basic composition of samples and weight percentage of the elements, represented by EDX analysis

Sample	The weight percentage of elements %						
	N	O	Na	Si	P	S	Ca
BAG/CMC NC	8.41	39.18	37.67	3.98	0.97	8.74	1.05
BAG/β-CD NC	3.95	39.71	2.77	2.77	24.51	0.73	25.56
BAG/CMC/β-CD NC	7.67	37.39	26.99	9.12	1.40	12.11	5.32
BAG/CMC/β-CD NF	5.31	33.18	8.72	7.79	2.99	38.94	3.07

0–1200 eV, are shown in Fig. 6. Judging from the XPS survey spectrum in Fig. 6a, the sample is composed of N, O, Na, Ca, S, and Si elements. The photoelectron lines at binding energies of 400.66 eV, 531.80 eV, 1071.80 eV, 347.65 eV, 162.85 eV, and 103.85 eV correspond to N 1 s, O 1 s, Na 1 s, Ca 2p, S 2p, and Si 2p, respectively. The N 1s spectrum (Fig. 6b) could be fitted to two distinct peaks at 400.59 eV and 400.93 eV, corresponding to sp^2-hybridized nitrogen, sp^3-hybridized nitrogen, and amino functional groups with a hydrogen atom. The O 1s spectrum (Fig. 6c) shows a peak with a binding energy of 531.8 eV, corresponding to loosely bound hydroxyl groups attached to the surface of nanofibers. After deconvolution, the Na 1s spectrum in Fig. 6d displays two broad peaks located at 1071.80 and 1073.22 eV, which correspond to the atomic sodium. Two major peaks attributed to Ca 2p are observed at binding energies of 347.80 and 350.65 eV with a peak separation of 3.5 eV (Fig. 6e). The S 2p spectrum in Fig. 6f displays two peaks located at 162.66 eV and 162.71 eV, which are attributed to the –SO– bond. From Fig. 6g, the Si 2p spectrum can be fitted into two peaks at 104.21 eV and 103.67 eV, attributed to the elemental silicon and silicon dioxide [41, 42].

BET Specific Surface Area

The BET-specific surface area and porous nature of BAG/CMC/β-CD NF, analyzed by N_2 adsorption–desorption isotherms, are shown in Fig. 6h. Its mesoporous structure is revealed by a typical IV-type isotherm with an H3 hysteresis loop in the range of $P/P_0 > 0.4$, as well as the pore-size distribution curve (the inset of Fig. 6h). The BET-specific surface area and total pore volume are estimated to be 23.17 $m^2 g^{-1}$ and 0.01 $cm^3 g^{-1}$, respectively. The high surface-to-volume ratio and porosity of BAG/CMC/β-CD NF make it favorable candidate for drug delivery as it provides a large contact area for loading. They also enhance affinity to molecules. When the affinity is high, an initial burst of high dosage of a drug can be prevented, and a low sustained rate of drug release can be obtained, which is beneficial [29].

Morphological Studies

Surface morphologies of BAG/CMC, BAG/β-CD, BAG/CMC/β-CD NCs, and BAG/CMC/β-CD NF, examined by the FESEM technique at three magnification ranges, are presented in Fig. 7. FESEM images in Fig. 7a–f show irregular planar and stacked lamellar structures of BAG/CMC and BAG/β-CD samples, observable porosity, and a large number of in-plane holes. FESEM images of BAG/CMC/β-CD NC in Fig. 7g–i reveal the smooth spherical nanoparticles in a mass structure without marks of cracking. FESEM images of BAG/CMC/β-CD NF in Fig. 7j–l display a strand structure with a smooth surface. Electrospun nanofibers provide a promising structure for high loading of target drug molecules [30].

TEM images of BAG/CMC/β-CD NF are shown in Fig. 8a–f. The images show the cross-linked nanofibers with a relatively equal diameter of about 10 nm. The nanofiber chains have been entangled to create a uniform and complex composition.

Quantitative Investigations on Flutamide-Loaded BAG/CMC/β-CD NF

Preparation of Calibration Curve by UV–Vis Spectrophotometric Analysis

The most reported methods to determine a correct drug content are HPLC or liquid chromatographic techniques utilizing UV, fluorescence, and electrochemical detectors. These methods are expensive, complicated, and involve prolonged extraction procedures [43]. The simple, sensitive, and cost-effective method is UV–Vis spectroscopy to study drug content, loading efficiency, and in vitro drug release as applied in this work for quantitative investigations on flutamide-loaded BAG/CMC/β-CD NF [44]. By dissolving 1.5 mg of flutamide in 2.5 mL of methanol and then adding phosphate buffer medium with pH 7.4 in a 50 mL volumetric flask, a stock solution (30 mg/L) was prepared. Six solutions with different concentrations were prepared by transferring aliquots from the stock solution into separate 50 mL flasks and diluting the volume with the medium. The absorbance of these solutions was measured at $\lambda_{max} = 282$ nm using a UV–Vis spectrophotometer. Based on the results listed in Table 3, the standard flutamide calibration curve was created, as demonstrated in Fig. 9a. The linear regression

Fig. 6 a XPS survey scan spectrum of BAG/CMC/β-CD NF and its fitted spectrum of **b** N 1s, **c** O 1s, **d** Na 1s, **e** Ca 2p, **f** S 2p, and **g** Si 2p. **h** Nitrogen adsorption–desorption isotherms of BAG/CMC/β-CD NF. The inset figure shows the pore-size distribution curve of BAG/CMC/β-CD NF
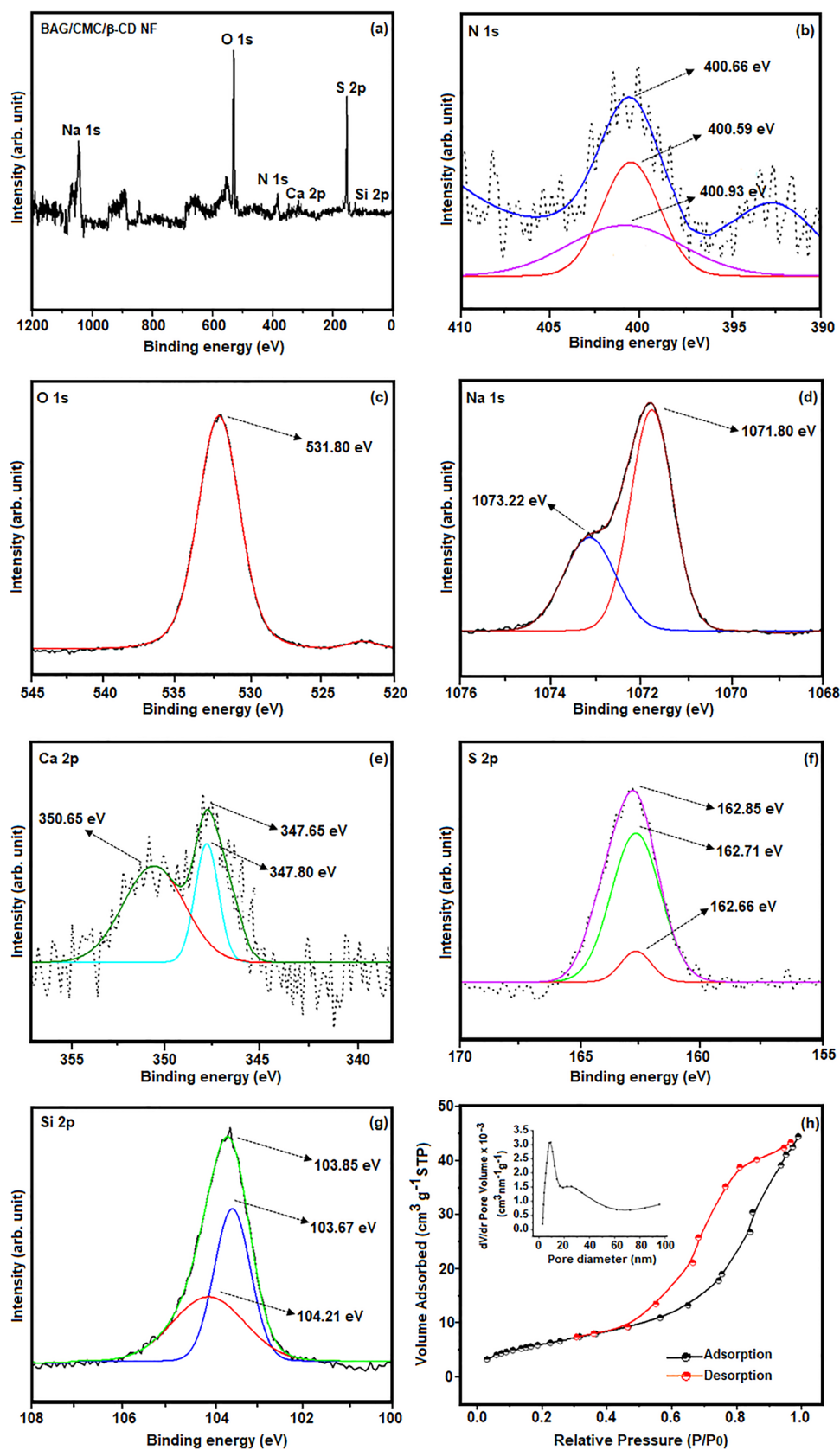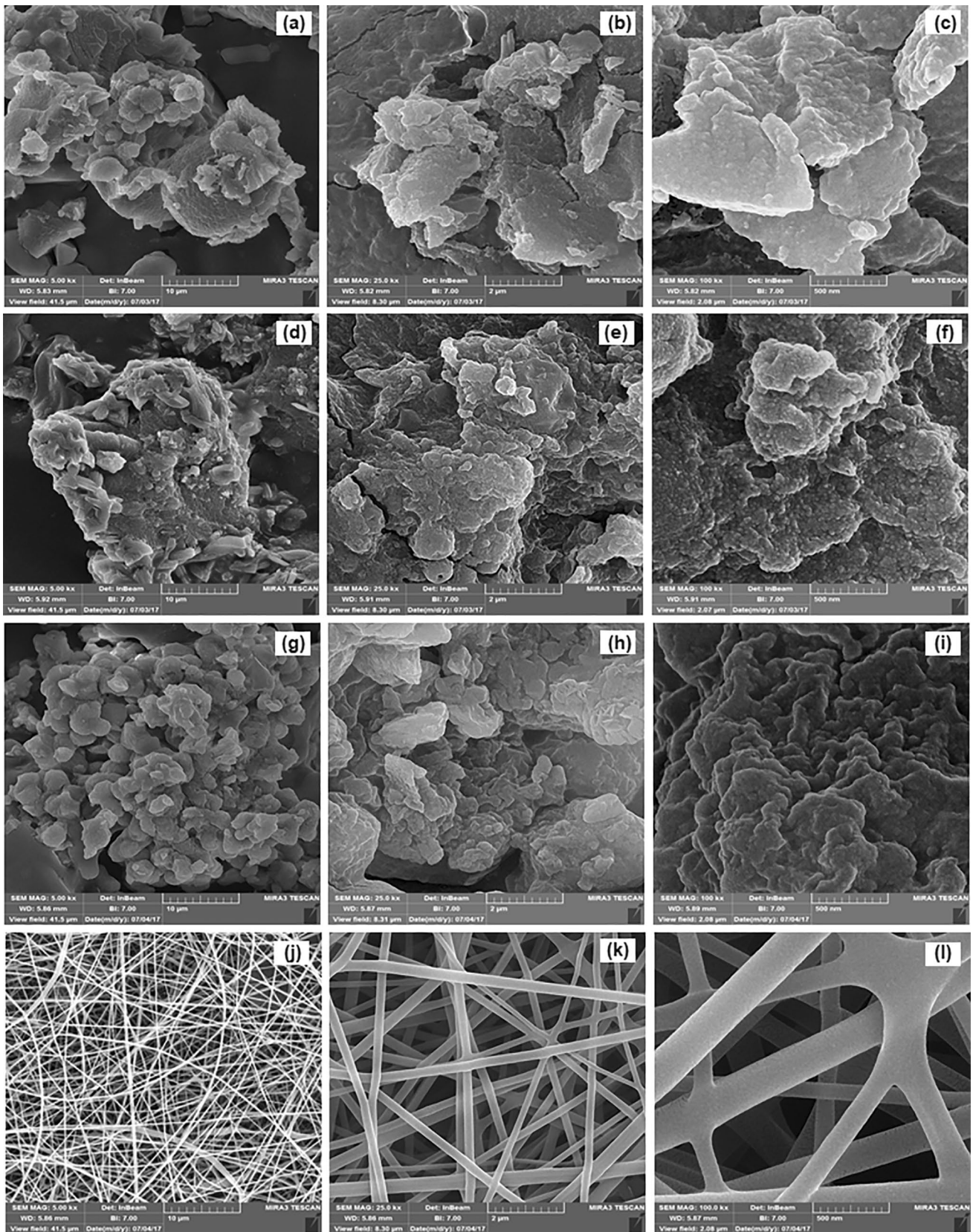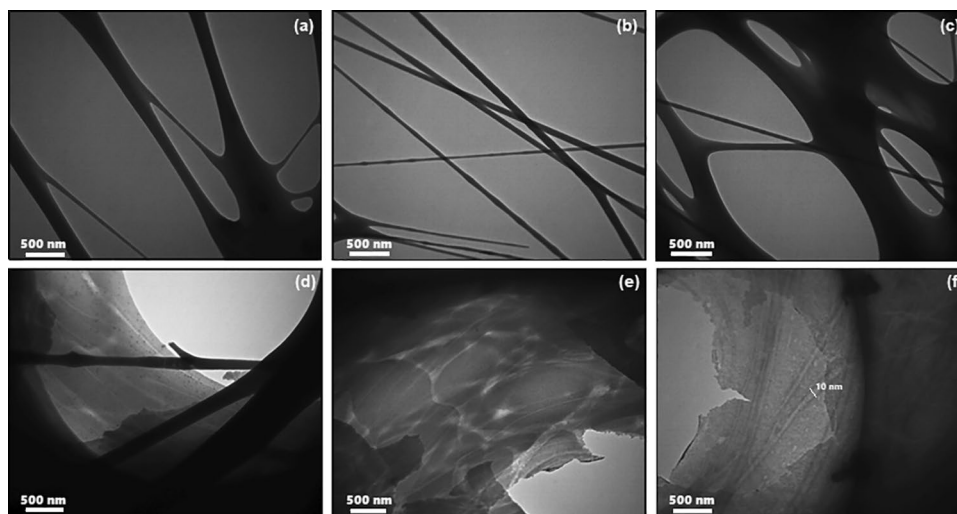
Fig. 7 FESEM images of **a–c** BAG/CMC NC, **d–f** BAG/β-CD NC, **g–i** BAG/CMC/β-CD NC, and **j–l** BAG/CMC/β-CD NF

Fig. 8 **a–f** TEM images of BAG/CMC/β-CD NF

obtained by the following equation resulted in a regression coefficient (R^2) value of 0.9995:

$$y = 0.038x + 0.1817, \qquad (2)$$

where y is the absorbance measured at $\lambda_{max} = 282$ nm and x is the concentration of flutamide (mg/L).

Determination of Flutamide Loading Efficiency (DL%)

According to the procedure, 1 mg flutamide drug was dissolved in 2.5 mL methanol and added to 150 mL phosphate buffer with pH 7.4. Then, 3 mg BAG/CMC/β-CD NF was mixed with the solution and stirred for 24 h at 5000 rpm using a magnetic stirrer. The mixture was then centrifuged and dried by a freeze-dryer. The absorbance of the incorporated drug detected in the solution was measured at 282 nm using a UV–Vis spectrophotometer. A value of 0.261 was obtained. Based on the above curve and the given equation, the concentration of the drug detected in the solution was calculated to be 2.08 mg/L. The drug loading efficiency (DL%) was then defined using this equation:

$$DL(\%) = (C_i - C_f) / C_i \times 100, \qquad (3)$$

**Table 3** Absorbance of dilute drug solutions in phosphate buffer (mg/L)

Absorbance	Concentration (mg/L)
0.224	1
0.297	3
0.365	5
0.445	7
0.564	10
0.753	15

where C_i and C_f are the initial concentration of the drug and the concentration of the incorporated drug detected in the solution, respectively. The flutamide drug loading efficiency on BAG/CMC/β-CD NF was determined to be 99.65%.

Determination of Flutamide Release Efficiency (DR%)

The flutamide drug has a non-steroidal structure and produces fewer hormonal side effects than the other drugs. However, due to the rare side effects of acute hepatotoxicity, it should be taken in lower doses at longer intervals. A desirable sustained dosage form should release about 70–90% of flutamide within 8–10 h. The sustained drug release ensures a constant drug plasma level and maximum time in the systemic circulation, leading to more efficient drug absorption and ultimately improving patient compliance. In general, the drug release behavior of the nanofibers, which is greatly influenced by the drug-matrix arrangement, can avoid drug level fluctuations, toxic accumulation, and multiple dosages. The drug release is characterized by three phases: (1) an initial phase, which could be rapid release (burst effect) or slow release, depending on the release kinetic models of drug molecules from the matrix surface. It is governed by drug dissolution and disintegration in the water or media penetrating the matrix and the erosion of the matrix. (2) A phase where the release of the drug would be approximately linear with respect to time. (3) A final phase is when drug release is tapered off as the initial drug concentration in the matrix decreases and the diffusion of the remaining drug molecules inside the matrix becomes more difficult. Different studies have shown that hydrophilic matrices have the potential to control and sustain the release of drugs. It has been observed that the quantity and rate of drug release are inversely proportional to the percentage of hydrophilic matrix [45].

Fig. 9 **a** The standard flutamide calibration curve, **b** absorption diagram versus the concentration of flutamide detected in a buffer solution over a period of 48 h, and **c** drug release percentage in phosphate buffer solution per time (hour)
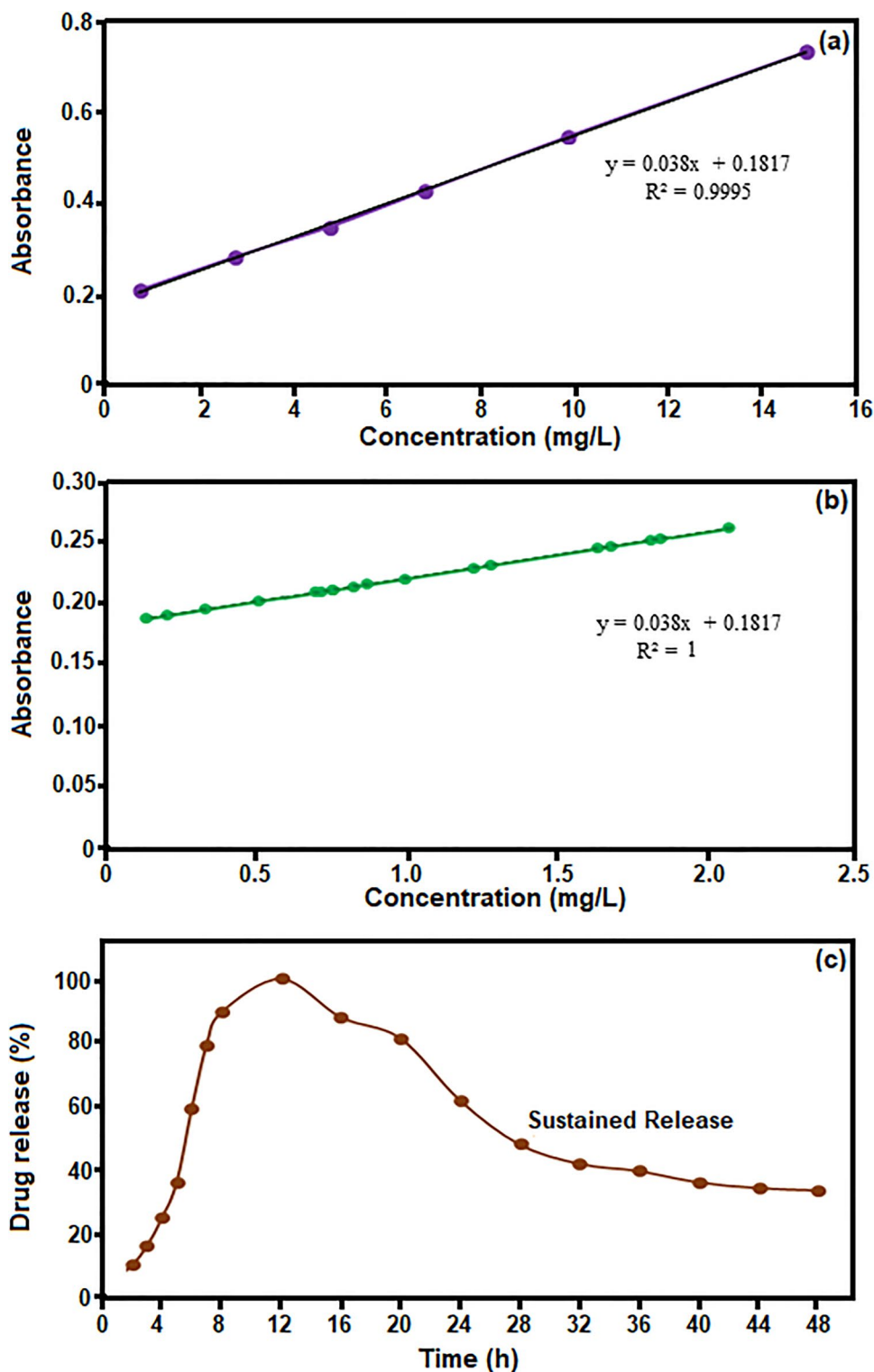
This study monitored the release efficiency of flutamide in a simulated intestinal environment. Accordingly, a solution was prepared by adding 6 mg of the freeze-dried flutamide-loaded BAG/CMC/β-CD NF to 10 mL phosphate buffer with a pH of 7.4. The solution was then placed in a shaker and stirred at a rate of 90 rpm for 45 min. At regular intervals for 8 h (approximately every 1 h), 0.5 mL aliquots of the sample were taken out by a sampler, centrifuged at 3000 rpm for 5 min, and the absorbance of the supernatants was measured at 282 nm. The additional solution was then returned back to the stock in the beaker. Using a high buffer-to-sample volume ratio helps to maintain the constant volume. After 8 h,

Table 4 Release of drug solution in phosphate buffer with a pH of 7.4

Time (h)	Absorbance	Concentration of the released drug (mg/L)	Drug released (%)
1	0.187	0.145	6.96
2	0.190	0.216	10.36
3	0.195	0.342	16.41
4	0.202	0.524	25.14
5	0.210	0.758	36.37
6	0.229	1.234	59.21
7	0.244	1.653	79.32
8	0.253	1.866	89.54
12	0.261	2.084	100
16	0.251	1.834	88.01
20	0.246	1.697	81.43
24	0.231	1.292	61.99
28	0.220	1.005	48.22
32	0.215	0.879	42.18
36	0.213	0.831	39.87
40	0.210	0.758	36.37
44	0.209	0.721	34.60
48	0.208	0.705	33.83

0.5 mL aliquots of the sample were taken out every 4 h until 40 h (10 times), and the steps were repeated again. Based on the data recorded in Table 4, an absorption diagram versus the concentration of flutamide detected in a buffer solution over a period of 48 h was created, as shown in Fig. 9b. The results indicated that the release mechanism of flutamide was dependent on time. The drug release efficiency (DR%) was determined using the following fitting:

$$DR(\%) = (M_t/M_n) \times 100, \tag{4}$$

where M_t is the concentration of the drug released in each stage, and M_n is the highest concentration of the released drug. Figure 9c shows the drug release percentage versus time (h), indicating that flutamide is released in the initial few hours, achieving 100% release within 12 h, and followed by a sustained release pattern, which is due to the slow

degradation of the matrix. These findings suggest that BAG/CMC/β-CD NF have a high loading efficiency and sustained drug release capacity, without an initial burst release, making them a promising candidate for flutamide drug delivery. Table 5 compares the release patterns of flutamide in several drug delivery systems at a pH of 7.4.

Drug Release Mechanism

Understanding the relationship between the structure and function is required to design a customized drug delivery system. In literature, electrospun nanofibers have been used to employ different release profiles, including immediate, sustained, prolonged, delayed, on-demand, and multiple-phase releases strategies [50]. These profiles can be achieved during electrospinning (Encapsulation) or post-electrospinning through physical adsorption, chemical bonding, and coating to enhance the drug solubility and loading efficiency, avoid drug degradation, and deliver the drug in a directed or continuous manner [51]. Nevertheless, there are still challenges in precisely controlling the release rate and duration due to diffusion limitations [52]. The drug release mechanism through nanofibers is a complex process that depends on multiple factors: (1) the physicochemical properties of the drug such as solubility, stability, molecular size, and chemical interaction of the drug with the matrix, (2) the structural characteristics of the matrix such as morphology, specific surface area, porosity, size, and (3) the physiological conditions, such as pH, temperature, ionic strength, and enzymes existing in the media. To further understand the drug release mechanism, the Korsmeyer–Peppas semi-empirical model is commonly used:

$$\log (M_t/M_\infty) = \log k + n \log t, \tag{5}$$

where M_t is the quantity of released drug at the time t, M_∞ is the maximum quantity of released drug (at equilibrium), k is the kinetic constant related to the properties of the drug delivery system, and n is the release exponent. Based on the plot of $\log (M_t/M_\infty)$ against $\log t$, the slope of the graph represents the value of n, while the intercept of the lines represents the value of k. The drug release mechanism can

Table 5 Sustained release patterns of flutamide in several drug delivery systems at a pH of 7.4

Flutamide delivery system	Drug loading (%)	Drug released (%)	Time (h)	References
ACMO/AA-based hydrogels	50	30	24	[45]
PLGA-PEG-Praz nanoparticles	69	100	30	[46]
CS-DS nanoparticles	55	66	120	[47]
PAMPA nanomicelles	94	86	10	[48]
AlN nanoparticles	67	28	48	[49]
BAG/CMC/β-CD nanofibers	~100	100	12	Current work

Fig. 10 **a** Comparison of FT-IR spectrum of flutamide-loaded BAG/CMC/β-CD NF with that of BAG/CMC/β-CD NF, **b** EDX spectrum of flutamide-loaded BAG/CMC/β-CD NF, the inset of figure **b** exhibits the chemical structure of flutamide. FESEM images of BAG/CMC/β-CD NF **c** 500 nm and **d** 200 nm magnification ranges
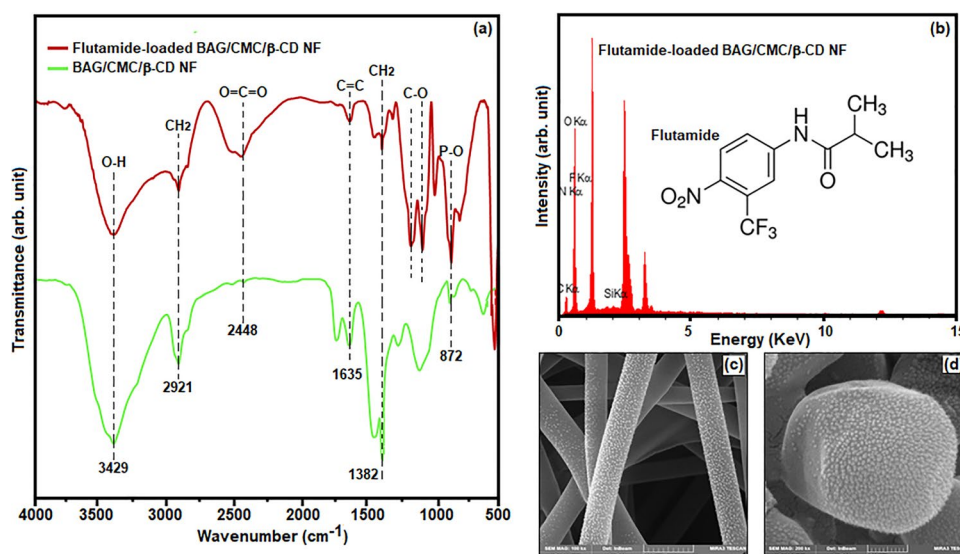
be governed by the Fickian diffusion when $n \leq 0.45$, or the non-Fickian anomalous mechanism when $0.45 < n < 0.89$ (case I), or controlled by polymer relaxation when $n > 0.89$ (case II). In this work, the drug release mechanism with n value of 0.3 follows the Fickian diffusion law. Drug release mechanism through nanofibers is mainly a diffusion-driven process, depending on the type of polymer used. Biodegradable polymers typically follow the Fickian diffusion, while non-degradable or complex polymeric systems may exhibit non-Fickian behavior [45, 50].

Physicochemical Analyses

When trying to load a drug onto electrospun nanofibers, it is essential to take into account the physicochemical properties of the nanofibers, as well as their interaction with the drug molecules. These factors significantly impact drug loading efficiency and drug kinetics release. In Fig. 10a, the FT-IR spectrum of flutamide-loaded BAG/CMC/β-CD NF is compared with that of BAG/CMC/β-CD NF. The analysis reveals that the flutamide drug has been immobilized on the surface of electrospun BAG/CMC/β-CD NF, and due to the chemical modification and reactive functional groups, it is not easily leached out. Different functional groups such as C–H, C=C, C=O, and O–H are employed to bind flutamide molecules onto the surface of nanofibers via Van der Waals forces, covalent bonds, and hydrogen bonding, which are also desirable for the drug loading [53].

The chemical composition of flutamide-loaded BAG/CMC/β-CD NF, evaluated through the EDX spectrum, is shown in Fig. 10b. The elemental analysis confirms the presence of the expected elements of C, N, O, Si, and F available in the nanofibers and the flutamide drug. The inset of Fig. 10b exhibits the chemical structure of flutamide.

The internal structures of nanofibers play a crucial role in achieving desired drug loading and release profiles. Two surface morphologies of flutamide-loaded BAG/CMC/β-CD NF, examined by the FESEM technique at 500 nm and 200 nm magnification ranges, are presented in Fig. 10c, d, respectively. No morphological change is observed after the modification. Flutamide-loaded BAG/CMC/β-CD NF have a complex and heterogeneous structure using the sandwich technology, where one layer of flutamide-loaded nanofibers is covered with another layer of nanofibers without flutamide, making a barrier for immediate drug release. Electrospun nanofibers provide a promising structure for the loading of drug molecules with sustained drug release properties. The images show that BAG/CMC/β-CD NF has succeeded in achieving high drug loading and prolonged drug release.

Conclusions

In summary, novel BAG/CMC/β-CD nanofibers, fabricated through the electrospinning process, were used as a drug delivery system. The simple setup, ease of operation, inherent high surface-to-volume ratio, cost-effectiveness, and many attractive features of electrospinning were effective in achieving bioactive glass nanofibers. The flutamide anticancer drug molecules were successfully incorporated onto the surface of nanofibers under in vitro conditions, resulting in a high drug loading efficiency of 99.65% and a sustained drug release without any initial burst release. Various analytical techniques characterized the structure, composition, and morphology of the synthesized samples. The results of this study are significant in the biomedical field, as they demonstrate the potential of electrospun bioactive glass

nanofibers for lower-dose drug administration in the treatment of cancers. Future studies on the loading of other drugs and their broad practical applications hold promise for next-generation treatment options.

Author Contributions We confirm that all the authors named in the manuscript have read and approved it. Professor MS-S and Professor KZ oversaw all experiments and research activities, including experiment design, data interpretation, and manuscript preparation. MT, author of the manuscript, prepared figures, tables, and graphical design, synthesized nanobioceramics and nanofibers, conducted experiments and data interpretation. NF as a consultant conducted experiments, research and data collection.

Data Availability Not applicable. All of the mentioned data including XRD, FT-IR, XPS, UV–Vis, BET, FESEM, EDX, and TEM have been collected in the chemistry lab of Olum Tahghighat Branch, Islamic Azad University and not been published previously. Also, the quotes have been cited in the Reference section.

Declarations

Conflict of interest We confirm that all authors named in the manuscript have read and approved it. In addition, there are no other individuals who meet the criteria for authorship. Throughout the Editorial process (including communication with the Editorial Manager and directly with the office), the Corresponding Author is the sole point of contact. Mirabdullah Seyed-Sadjadi is responsible for communicating with the other authors about progress, revisions, and final approvals of proofs. It has been confirmed that the Corresponding Author's email address is current and accurate.

Ethics approval and consent to participate Not applicable. The reported research does not have any animal or human data or tissue.

Consent for publication Not applicable. The manuscript does not contain data from any person.

References

1. H.E. Skallevold, D. Rokaya, Z. Khurshid, M.S. Zafar, Int. J. Mol. Sci. **20**, 5960 (2019)
2. E. Moon, E. Kang, W. Song, B.J. Kim, H.J. Cha, Y.S. Choi, Korean J. Chem. Eng. **40**, 405 (2023)
3. J.R. Jones, Acta Biomater.Biomater. **9**, 4457 (2013)
4. J. Feng, E.S. Thian, Nanotechnol. Rev.. Rev. **2**, 679 (2013)
5. L.L. Hench, J. Eur. Ceram. **29**, 1257 (2009)
6. T. Kokubo, Biomater. **12**, 155 (1991)
7. M.N. Rahaman, D.E. Day, B.S. Bal, Q. Fu, S.B. Jung, L.F. Bonewald, A.P. Tomsia, Acta Biomater.Biomater. **7**, 2355 (2011)
8. F. Baino, G. Novajra, V. Miguez-Pacheco, A.R. Boccaccini, C. Vitale-Brovarone, J. Non-Cryst, Solids **432**, 15 (2016)
9. F. Xie, I. Gonzalo-Juan, M. Arango-Ospina, R. Riedel, A.R. Boccaccini, E. Ionescu, A.C.S. Biomater, Sci. Eng. **5**, 5337 (2019)
10. D. Zhang, O. Leppäranta, E. Munukka, H. Ylänen, M.K. Viljanen, E. Eerola, L. Hupa, J. Biomed. Mater. Res. Part A **93**, 475 (2010)
11. L. Drago, E.D. Vecchi, M. Bortolin, M. Toscano, R. Mattina, C.L. Romanò, Future Microbiol.Microbiol. **10**, 1293 (2015)
12. S. Kargozar, M. Montazerian, S. Hamzehlou, H.W. Kim, F. Baino, Acta Biomater.Biomater. **81**, 1 (2018)
13. V. Miguez-Pacheco, L.L. Hench, A.R. Boccaccini, Acta Biomater. Biomater. **13**, 1 (2015)
14. J. Kraxner, M. Michalek, A.R. Romero, H. Elsayed, E. Bernardo, A.R. Boccaccini, D. Galusek, Mater. Lett. **256**, 126625 (2019)
15. S.K. Sarkar, B.T. Lee, Bioceram. Dev. Appl.. Dev. Appl. **1**, 1 (2011)
16. Y. Wang, X. Chen, Mater. Lett. **189**, 325 (2017)
17. B.A. Ben-Arfa, R.C. Pullar, Processes **8**, 615 (2020)
18. H.S. Yun, S.H. Kim, S. Lee, I.H. Song, Mater. Lett. **64**, 1850 (2010)
19. M. Cannio, D. Bellucci, J.A. Roether, D.N. Boccaccini, V. Cannillo, Mater. **14**, 5440 (2021)
20. K. Zheng, A.R. Boccaccini, Adv. Colloid Interface Sci. **249**, 363 (2017)
21. J. Zhong, D.C. Greenspan, J. Biomed. Mater. Res. **53**, 694 (2000)
22. A. Balamurugan, G. Sockalingum, J. Michel, J. Fauré, V. Banchet, L. Wortham, G. Balossier, Mater. Lett. **60**, 3752 (2006)
23. H.W. Kim, H.E. Kim, J.C. Knowles, Adv. Funct. Mater.Funct. Mater. **16**, 1529 (2006)
24. M.S. El-Okaily, A.M. El-Rafei, M. Basha, N.T.A. Ghani, M.M. El-Sayed, A. Bhaumik, A.A. Mostafa, Int. J. Biol. Macromol.Macromol. **182**, 1582 (2021)
25. W.E. Teo, R. Inai, S. Ramakrishna, Sci. Technol. Adv. Mater. (2011).
26. A. Allafchian, H. Hosseini, S.M. Ghoreishi, Int. J. Biol. Macromol.Macromol. **163**, 1780 (2020)
27. Z. Norouzi, M. Abdouss, Int. J. Biol. Macromol.Macromol. **233**, 123518 (2023)
28. S. Allahyari, N. Esmailnezhad, H. Valizadeh, M. Ghorbani, M. Jelvehgari, F. Ghazi, P. Zakeri-Milani, J. Drug Deliv. Sci. Technol. **61**, 102275 (2021)
29. R. Contreras-Cáceres, L. Cabeza, G. Perazzoli, A. Díaz, J.M. López-Romero, C. Melguizo, J. Prados, Nanomater. **9**, 656 (2019)
30. K. Ye, H. Kuang, Z. You, Y. Morsi, X. Mo, Pharmaceutics **11**, 182 (2019)
31. R. Kamalian, A. Yazdanpanah, F. Moztarzadeh, R. Ravarian, Z. Moztarzadeh, M. Tahmasbi, M. Mozafari, Ceram. Silik.Silik. **56**, 331 (2012)
32. Y. Rezaei, F. Moztarzadeh, S. Shahabi, M. Tahriri, Synth. React. Inorg. Met-Org. Nano-Met. Chem. **44**, 692 (2014)
33. N. Nabian, M. Jahanshahi, S.M. Rabiee, J. Mol. Struct. **998**, 37 (2011)
34. M.A. Morsi, A.H. Oraby, A.G. Elshahawy, R.M. Abd El-Hady, J. Mater. Res. Technol. **8**, 5996 (2019)
35. R. Li, A.E. Clark, L.L. Hench, J. Appl. Biomater.Biomater. **2**, 231 (1991)
36. S. Talebian, M. Mehrali, S. Mohan, M. Mehrali, H.M. Khanlou, T. Kamarul, A.A. Abass, RSC Adv. **4**, 49144 (2014)
37. C. Gao, Q. Gao, Y. Li, M.N. Rahaman, A. Teramoto, K. Abe, J. Biomed. Mater. Res. Part A **100**, 1324 (2012)
38. L.B. Capeletti, I.M. Baibich, I.S. Butler, J.H. dos Santos, Spectrochim. Acta A Mol. Biomol. Spectrosc. **133**, 619 (2014)
39. J.P. Borrajo, S. Liste, J. Serra, P. González, S. Chiussi, B. León, M. Pérez-Amor, Key Eng. Mater. **284**, 465 (2005)
40. M.F. Zaky, E.A. Essa, A.A. Bosela, G.M. Maghraby, Eur. J. Biomed. Pharm. Sci. **5**, 12 (2018)
41. A.M. Deliormanlı, Ceram. Int. **41**, 417 (2015)
42. D. Cheng, R. Xie, L. Jin, M. Cao, X. Jia, Q. Cai, X. Yang, RSC Adv. **6**, 53958 (2016)

43. M.S. Kang, N.H. Lee, R.K. Singh, N. Mandakhbayar, R.A. Perez, J.H. Lee, H.W. Kim, Biomater. **162**, 183 (2018)

44. A. El-Fiqi, J.H. Kim, H.W. Kim, A.C.S. Appl, Mater. Interfaces **7**, 1140 (2015)

45. M.F. Abou Taleb, S. El-Sigeny, M. El-Kemary, Macromol. Res.. Res. **20**, 407 (2012)

46. A. Fattahi, M. Ghiasi, P. Mohammadi, L. Hosseinzadeh, K. Adibkia, G. Mohammadi, Braz. J. Pharm. Sci., **54** (2019).

47. A. Anitha, S. Uthaman, S.V. Nair, R. Jayakumar, V.K. Lakshmanan, J. Biomed. Nanotechnol.Nanotechnol. **9**, 335 (2013)

48. R. Mirsafaei, J. Varshosaz, IET Nanobiotechnol.Nanobiotechnol. **14**, 417 (2020)

49. X. Gong, L. Guo, R. Zhou, Inorg. Chem. Commun.Commun. **158**, 111478 (2023)

50. M.K. Gaydhane, C.S. Sharma, S. Majumdar, RSC Adv. **13**, 7312 (2023)

51. Z. Jiang, Z. Zheng, S. Yu, Y. Gao, J. Ma, L. Huang, L. Yang, Pharm. **15**, 1829 (2023)

52. X. Duan, H.L. Chen, C. Guo, J. Mater. Sci. Mater. Med. **33**, 78 (2022)

53. J. Hum, A.R. Boccaccini, J. Mater. Sci. Mater. Med. **23**, 2317 (2012)